Article

THE POWDER OF $Co_{64}Nb_{30}B_6$ OBTAINED BY MECHANICAL ALLOYING

Luciano Nascimento[a,*], Ítallo Campos Gonçalves de Morais[a], Adriano Lima da Silva[a], João Baptista da Costa Agra de Melo[b], Danyelle Garcia Guedes[a], Lincoln Rodrigues Sampaio de Araújo[c], Suédina Maria de Lima Silva[a] and Ana Cristina Figueiredo de Melo Costa[a]

[a]Departamento de Engenharia de Materiais, Universidade Federal de Campina Grande, 58429-900 Campina Grande – PB, Brasil
[b]Departamento de Engenharia Mecânica, Universidade Federal de Campina Grande, 58429-900 Campina Grande – PB, Brasil
[c]Departamento de Física, Universidade Federal de Campina Grande, 58429-900 Campina Grande – PB, Brasil

Received: 07/28/2023; accepted: 01/10/2024; published online: 03/18/2024

This work aims to synthesize the alloy $Co_{64}Nb_{30}B_6$ through mechanical alloying using a planetary ball mill. A disc rotation *per* minute and a ball/powder weight ratio of 300 rpm and 10:1 were used, with a milled time of 10 h, respectively. The characterization of the $Co_{64}Nb_{30}B_6$ alloy was performed by X-ray diffraction (XRD), examined by scanning electron microscope-energy dispersive X-ray spectroscopy (SEM-EDS), thermoanalytical techniques (TGA/DTA), vibrating sample magnetometer (VSM) and confirmed by Braunauer, Emmet e Teller (BET) method type IV isotherms with a hysteresis loop for mesoporous materials. The results indicated that the evolution of the amorphous phase in the $Co_{64}Nb_{30}B_6$ composition through the mechanical alloying process exhibited good soft magnetic properties with the addition of the metalloid element B and its excellent unique ferromagnetic properties. Through thermoanalytical analysis (TGA/DTA), it was shown that at higher temperatures, Co and Nb ions are oxidized by the environment and, therefore, the mass can be slightly increased to 14.9% and a probable contribution of boron in evolution stability thermal and magnetic in the amorphous phase, respectively. This suggests that the newly developed high-performance amorphous alloy $Co_{64}Nb_{30}B_6$ has great application potential.

Keywords: amorphous alloy $Co_{64}Nb_{30}B_6$; mechanical alloying; characterization.

INTRODUCTION

Since their discovery in 1960, amorphous alloys were first synthesized in the 1960s by Pol Duwez, using the rapid quenching method technique at a system binary metallic alloy $Au_{80}Si_{20}$ and even after five decades, their potential has yet to be fully revealed. Using the binary alloy $Au_{80}Si_{20}$, through the processing method melt spinning, with a cooling rate of approximately 10^5-10^6 K s^{-1}, showed that the process of nucleation and growth of the crystalline phase can be kinetically avoided in some alloys.[1] Since then, many studies have focused on the processing of various amorphous metal alloy systems with different applications at the industrial level. Co-based amorphous alloys have excellent high saturation magnetization (m_s),[2] exhibit greater corrosion resistance,[3] demonstrate excellent mechanical properties,[4] high permeability (μ),[5] low coercivity (H_c),[6] low magnetic loss,[7] fast flux reversal,[8] and low acoustic loss due to their soft-magnetic properties used for fabrication of electronic components,[9] sensors devices and application in biomaterials.[10,11] The Co-based alloy can be used as a biomedical material due to its corrosion resistance, good biocompatibility, and outstanding mechanical properties.[12] Notably, however, the applications of cobalt alloys as orthopedic implants have presented a strong potential for applications in biomaterials. Co-based amorphous alloys have metastable phases obtained at low cooling rates, by which the free energy is more significant than that of the crystalline state.[13] This energy difference is the reason for a phase transition towards the crystalline phase, but a reduction of free energy may not result in better stability.[14] Furthermore, the mobility of atoms, represented by the activation energy, dominates the stability of the amorphous phase, inducing a process of amorphization.[15] The conditions of amorphization are closely linked to defects in the structure that raise its free energy to a level that exceeds the amorphous phase.[16]

*e-mail: luciano.uepb@gmail.com

However, due to their narrow hysteresis loop, Co-based amorphous alloys have a magnetocaloric effect near room temperature and minimal hysteresis losses.[17,18] Therefore, Co-based amorphous alloy magnetocaloric materials have second-order phase transitions, which are considered promising candidates for developing magnetic scaffolds in biomaterials.[19] The addition of metalloid elements (i.e., B, Si, Ge, Se, C, and P) plays an essential role in the enhancement of the bulk metallic glasses (BMGs) of Co-based amorphous alloys.[20] The radius of metalloid atoms is much smaller than transition metals, and their prominent role is to provide the necessary eutectic composition to reach the amorphous state.[21]

Remarkably, the B addition in Co-rich amorphous alloys is promising, due to its interaction with other alloying elements, like Co and Nb, which have a scope for improvement in the optimization of their amorphization, melt-spun microstructure, thermo-physical, and soft-magnetic properties.[22,23] Amorphous alloys have been produced *via* a series of techniques, such as the melt-spinning method,[24] water/gas atomization,[25] plasma chemistry and plasma processing,[26] and mechanical alloying.[27] Among these, mechanical alloying (MA) is a peculiar processing technique that can produce various alloy powders with intermetallic, amorphous, and quasicrystalline phases and high entropy alloys.[28]

The advantage of this method is that the powder production capacity is large, and the process parameters are easy to control. Therefore, it is a suitable method for industrial and research purposes. The use of mechanical alloying for high energy milling (HEM),[29] is a completely solid-state processing method that is not bound to phase diagrams and can produce many amorphous alloys, which cannot be produced by fast solidifying processing.[30]

In the present study, the $Co_{64}Nb_{30}B_6$ component system was mechanically alloyed to obtain amorphous powder, and milling was for 10 h to get the amorphous phase. The amorphous powders were milled for 10 h *via* a wet mechanical alloying route, using a

process control agent (PCA) to homogenize the powder and an argon atmosphere to prevent further oxidation during powder milling. The present work aimed to understand the milling time of 10 h was necessary to obtain the amorphous phase of the $Co_{64}Nb_{30}B_6$ alloy; the evolution of the amorphous powder morphology and microstructural, magnetic properties, and thermal stability are presented and discussed.

EXPERIMENTAL

The nominal composition of the amorphous alloy $Co_{64}Nb_{30}B_6$ (wt.%) was obtained from mixtures of pure crystalline powders of Co, Nb, and B (> 99.99% purity). The Co and B powders were purchased from Sigma-Aldrich (Merck, Brazil), and the Nb powders were donated by the Companhia Brasileira de Metalurgia e Mineração (CBMM).

During the processing, powders were weighed on a BK4000 Micronal balance with a resolution of 10^{-2} g of the chemical elements in the proportions corresponding to the nominal composition $Co_{64}Nb_{30}B_6$ and no subsequent periodic collection was carried out during the amorphous alloy preparation process. Mechanical alloying was performed in a high energy planetarium (Fritsch Pulverisette 5). It was used cylindrical jars of 77 mm diameter for 80 mm tall and spheres (20, 12, and 7 mm in diameter), both of which are tungsten spheres and jars. The entire set was milled for 10 h in an argon atmosphere to avoid oxidation and refrigerated at 25 °C to avoid possible phase transformations. The charge of the powder mixture was maintained at 20 g for all tests, the rotating impeller turned 250 rpm, and the weight ratio between the milling balls and the powder was around 10:1.

During the grinding process, it was not interrupted to remove a small amount of powder for subsequent determination of microstructural characterization and analysis of the amorphous phase. The adopted speed test was 300 rpm, and the grinding time was 10 h. Finally, *n*-hexane (C_6H_{14}) (2 mL) was used as a process control agent (PCA) for the homogenization of the powder in the alloying process, and an argon atmosphere to prevent further oxidation of the metal powders. The *n*-hexane (C_6H_{14}) was purchased from Chemicals Carvalhaes (Rio Grande do Sul, Brazil).

The analysis of the amorphous structure was performed by X-ray diffraction (XRD) with a Bruker diffractometer, model D2 Phaser, a copper radiation CuK_α ($\lambda = 1.54056$ Å), 0. 016° s^{-1} step size, and a time of 5 s, at 40 kV and 30 mA in a 2θ ranging from 10° ≤ 2θ ≤ 80°. The morphological aspect of the sample of amorphous alloy $Co_{64}Nb_{30}B_6$ powders was examined by scanning electron microscope-energy dispersive X-ray spectroscopy (SEM-EDS) in a VEGA 3 equipment, TESCAN, operating at 30 kV using a magnification of 100,000x to verify how efficient the inter-diffusion of the chemical elements present in the amorphous alloy powder. Thermogravimetric analysis (TGA/DTG) of the amorphous alloy $Co_{64}Nb_{30}B_6$ was performed in an analyzer thermostat, Shimadzu, model DTG-60H, with the rate heating time of 10 °C min^{-1}. We started the analysis of the temperature ranging from ambient to 1000 °C, using a nitrogen atmosphere with a gas flow of 50 mL min^{-1} and 10 mg of sample in an alumina crucible. The high field magnetization curves were measured by a Microsense model EZ 7 Vibrant Sample Magnetometer (VSM) subjected to magnetic fields up to 2.7 T (i.e., 27 kOe) and in the temperature ranging from 77 to 1000 K. The magnetization curves were analyzed using the method of least squares. The field magnetization was parallel to the length of the sample to minimize the demagnetization effect. The coercive force H_c of the rods was investigated using a coercimeter with a metallic alloy probe.

RESULTS AND DISCUSSION

The result of the XRD pattern of the $Co_{64}Nb_{30}B_6$ alloy during milling of the mechanical alloying process is shown in Figure 1, obtained from 10 h of milling.

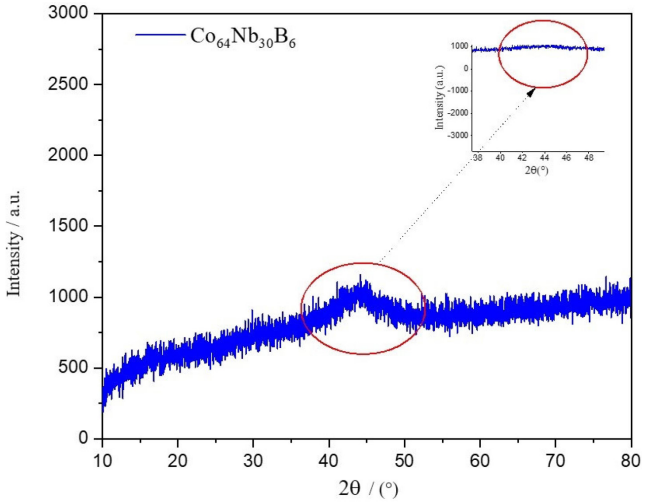

Figure 1. *XRD patterns of the $Co_{64}Nb_{30}B_6$ alloy milled from 10 h*

The halo peak inside the red circle corresponds to an amorphous phase structure that could be detected in the 2θ range of 35 and 50° (see Figure 1). In this case, no significant diffraction peak corresponding to the crystalline phase was observed, but only a diffraction pattern showing a typical diffuse amorphous halo peak with a maximum value at 2θ = 45° was observed. The diffraction pattern of the powders milled for more extended times does not show any appreciable changes. B is a metalloid, that is greatly used to stabilize the amorphous, magnetic and thermal phases during the mechanical alloying process.[31,32] Similar XRD results were observed in an amorphous XRD of Fe-Si-B powder and Fe-Si-B/SiO_2 composite powder, where a typical halo of amorphous structure, 2θ range of 40-50°, where a broad diffuse was observed with a maximum at 2θ = 45° that was mechanically milling between 200-250 rpm during 6 h of milling, respectively.[33]

Figure 2 shows (on the right) the SEM micrograph of the particles during the milling process of the amorphous alloy $Co_{64}Nb_{30}B_6$ with snowflake agglomerate morphology within the size of approximately 50 µm.

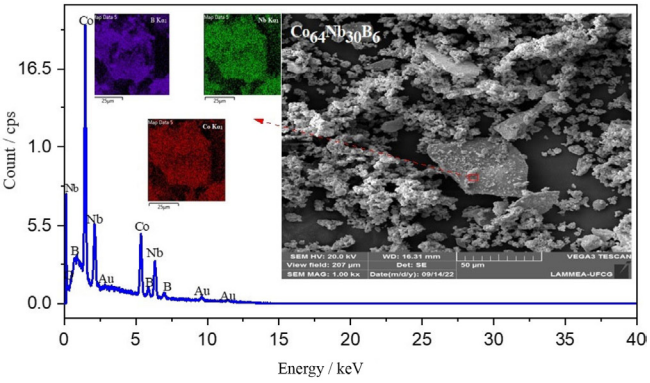

Figure 2. *SEM/EDS micrographs of $Co_{64}Nb_{30}B_6$ alloy milled from 10 h*

Repeated fracturing and cold welding occur throughout the milling process and generate the continual refinement of the particles. The 10 h-milled powders become refined obviously due to the

consecutive deformations, welding, and the fragmentation of particles with morphology's snowflake agglomerate and very irregular grains of about 50 μm.[34] Increasing the mechanical alloying time to 10 h, the large powder particles are further crushed, and the particle size difference decreases.

After milling for 10 h, the morphology of both powders became irregular but in the form of the snowflake agglomerate structures. Almost all of the particles have a granulometry of the grain size of 50 μm. After milling for 10 h and the speed 300 rpm (Figure 2), the milled powder develops into the agglomerated particles with a size of 50 μm, which are gradually increasing in snowflake shapes due to the cold welding phenomenon. The microstructure has irregular features due to the plastic deformation with the cracking of welded particles that work together to reduce particle size.[35] Figure 2 (to the left) shows the elemental composition (EDS) analysis of $Co_{64}Nb_{30}B_6$ amorphous alloy. The composition content of Co, Nb, and B was tested by EDS and shows that the distribution of metal atoms in the mechanical alloying process has been relatively uniform for the effect of amorphization.[36] Figure 3 shows the overlapping TGA/DTA curves for temperature range from ambient temperature to 1000 °C, that was measured in a nitrogen environment at a scanning rate of 10 °C min^{-1} of the $Co_{64}Nb_{30}B_6$ alloy.

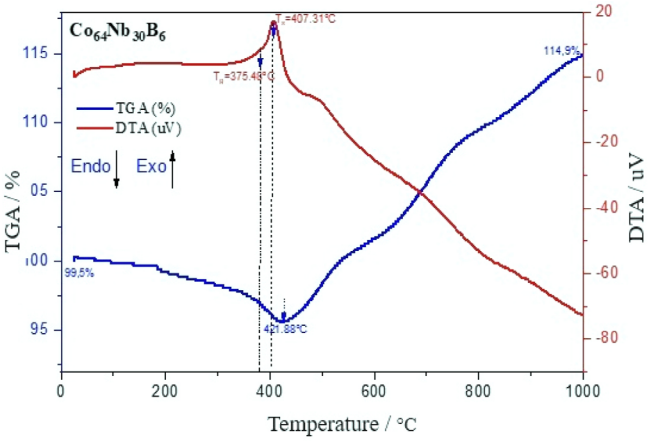

Figure 3. *Overlapping TGA/DTA curves of the $Co_{64}Nb_{30}B_6$ alloy milled from 10 h*

On the TGA curve, a small exothermic peak can be observed from 421.88 °C in the $Co_{64}Nb_{30}B_6$ alloy where there is a significant mass loss of ~ 96.35% as a consequence of the transformation of the remaining amorphous phase to the crystalline phase. The first exothermic peak in the DTA curve is located at about 407.31 °C, related to stress relaxation, recovery, and structural relaxation. The first exothermic reaction starts around 421.88 °C, which may be related to the crystallization of the amorphous phase. Compared with other similar amorphous alloys, from B in the alloy composition effectively increases the crystallization temperature and its thermal stability.

According to Figure 3, the glass transition temperature is T_g = 375.48 °C and the first crystallization temperature is around T_x = 407.31 °C from the amorphous alloy $Co_{64}Nb_{30}B_6$ tends to increase respectively as the Co and Nb contents increase with this stoichiometric variation of the composition of the chemical elements. At higher temperatures, both Co and Nb ions are oxidized by the environment and hence, the mass could be slightly enhanced to 14.9% (see Figure 3). It is assumed that the grain size might have increased since the ionic radius of Co (0.65 Å) is bigger than Nb (≈ 0.62 Å).[37] The sharpness of DTA peaks (Figure 3) developed with the increasing of Co and Nb content. As the temperature increases, pores are forming during the mechanical alloying process and resulting in the formation of an amorphous phase,[38] as shown in Figures 2 and 5.

The prominent exothermic peak at 421.88 °C in Figure 3 may be related to a small crystalline phase transformation during the crystallization process and a subsequent amorphous phase formation. From DTA curve of Figure 3, the crystallization temperatures peak (T_x) is around 407.31 °C, it rises with the growth of Co and Nb contents. In this inhomogeneous amorphous structure, a portion of the crystalline phase is formed in each region, which is characterized by the same composition short-range order as an amorphous region where this phase nucleates and grows, forming an agglomeration of the snowflake shape particles with approximately 50 μm. It was observed an exothermic peak at the maximum temperature of T_x = 407.31 °C, for the ground powder at 10 h in DTA curve of the amorphous alloy $Co_{64}Nb_{30}B_6$.

The glass transition temperature is T_g = 375.48 °C, crystallization starts at temperature T_x = 407.31 °C, and corresponds supercooled liquid region ($\Delta T = T_x - T_g$ = 31.83 °C) from the endothermic peak that was used to evaluate glass-forming ability (GFA) for of bulk metallic glasses (BMGs). This predominant exothermic peak represents a phase transformation existing in the alloy and transforms to a mixture of the nanocrystalline Co (Nb, B) phase diluted in the amorphous matrix. At the glass transition temperature of T_g = 375.48 °C, we note that the amorphous alloy $Co_{64}Nb_{30}B_6$ will transform into a supercooled liquid, suggesting that the glass transition temperature is an important parameter.

The exothermic temperature peak at T_x = 407.31 °C corresponds to crystallization events that can be observed and are associated with the transformations from an amorphous state to the equilibrium phases. The temperature of T_g = 375.48 °C indicates glass transition in the heating rate (see Figure 3). The DTA curve for the amorphous alloy $Co_{64}Nb_{30}B_6$, shows two discrete endothermic peaks at temperatures around 407,31 °C, which are related to stress and structural relaxation of powder ground during the milling process for 10 h.[39]

As shown in Figure 4, the M-H hysteresis loop of $Co_{64}Nb_{30}B_6$ alloy shows the typical behavior of soft magnetic materials.

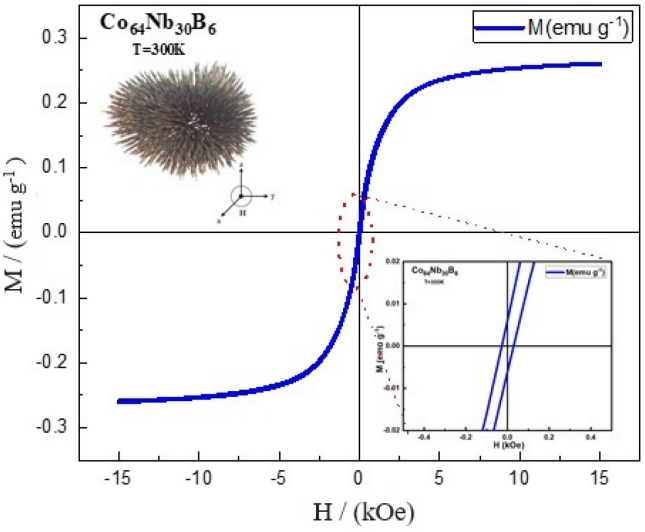

Figure 4. *Hysteresis loops M-H for the $Co_{64}Nb_{30}B_6$ alloy milled from 10 h*

From Figure 4, the saturated magnetization and coercivity value of this $Co_{64}Nb_{30}B_6$ alloy can be estimated as M_s = 0.2601 emu g^{-1} and H_c is very close to 287.68 kOe, respectively. The amorphous alloy $Co_{64}Nb_{30}B_6$ exhibits the low saturation magnetization of M_s = 0.2601 emu g^{-1} value, which is attributed to the highest Co and Nb content and the lowest B content. The high coercivity

(H_c = 28.68 kOe) of $Co_{64}Nb_{30}B_6$ alloy particles is due to the high structure anisotropy, owing to the disordered structure. The hysteresis curve in Figure 4 displays a typical behavior of ferromagnetic materials, that exhibit soft magnetic properties by forming a well-defined hysteresis loop.[40]

In the upper part of Figure 4, we can observe the milled powders strong ferromagnetic property of the amorphous alloy powder $Co_{64}Nb_{30}B_6$ display sigmoidal hysteresis curves as those that are typically seen in nanostructured materials with small magnetic domains obtained by mechanical alloying (MA). In addition, the illustration in the lower right corner of Figure 4 also shows that its field coercivity tends to decrease. The alloy $Co_{64}Nb_{30}B_6$ (Figure 4) shows saturation magnetization values of M_s = 0.2601 emu g^{-1} and remaining M_r = 0.00617 emu g^{-1}, respectively.

The identity of the value from the specific saturation magnetization M_s = 0.2601 emu g^{-1} of the powder from $Co_{64}Nb_{30}B_6$ is explained by a slight difference between the magnetizations of amorphous and crystallized phases (not more than 30%) and a negligible contribution to the total magnetization in the powder agglomerates of snowflakes. The most noticeable effect is revealed in the coercive field (H_c = 28.68 kOe) in alloy powder $Co_{64}Nb_{30}B_6$.

Based on this analysis of the magnetization curve, it is possible to verify the presence of linear defects, which indicates the presence of amorphous phases.[41] One can see an absence of magnetocrystalline anisotropy due to the existence of an amorphous phase structure in Figure 1. Amorphous materials exhibit low coercivity, which is actually due to the absence of mass-effective magnetocrystalline anisotropy, as their soft magnetic properties are controlled by voltage and magnetostriction coefficient.[42]

Since Co has a higher affinity for B, an enriched amorphous phase can be formed with B and Co, which has a negative magnetostriction.[43] We observe a sharp transformation of magnetostriction that can happen with an increase in the annealing temperature (recrystallization annealing) in the critical temperature vicinity of the irreversibility of this process. It can be assumed that the cause was the amorphous phase decomposition. The saturation magnetization of M_s = 0.2601 emu g^{-1} (shown in Figure 4) decreases, as expected, due to the dilution of the main magnetic component of the alloy $Co_{64}Nb_{30}B_6$ with the Co and Nb atoms.[44] Although $Co_{64}Nb_{30}B_6$ amorphous alloys present a low saturation magnetization value of M_s = 0.2601 emu g^{-1}, moderate use of Co and metalloid as alloying elements can confer benefits such as increased Curie temperature and enhanced glass-forming ability to the alloy system without affecting soft magnetic properties, increasing thermal stability and preventing the precipitation of secondary phases that affect the soft magnetic behavior of the alloys.

There is a higher domain wall movement related to its magnetic moment from the Co, increasing the coercivity for H_c = 28.68 kOe.[45,46] Some Co-based alloys have soft magnetic properties that are analyzed based on their initial permeability (μ_i) and effect permeability (μ_e). Alloys that exhibit excellent soft magnetic properties must be high μ_e above 20.000.[47] Fe-Co-B and Fe-P-B-Si-based amorphous alloy exhibits good soft magnetic properties, with a low coercivity (H_c) of 3.6 A m^{-1}, high effective permeability of 15000 at 1 kHz, and high saturation magnetization (B_s) above 1.8 T which were obtained by various metallurgical manufacturing process techniques.[48]

There are adsorption/desorption isotherms of N_2 of nitrogen at a temperature of 77 K for the amorphous alloy $Co_{64}Nb_{30}B_6$ as shown in Figure 5. The hysteresis loop of the black and red lines represents the adsorption (ADS) and desorption (DES) curves.

The hysteresis loop illustrated in Figure 5 for the amorphous alloy $Co_{64}Nb_{30}B_6$ shows a distinct hysteresis loop, indicating a high density of IV-type isotherm is typically characteristic of a mesoporous adsorbent and hysteresis loop H3 curve, as *per* IUPAC

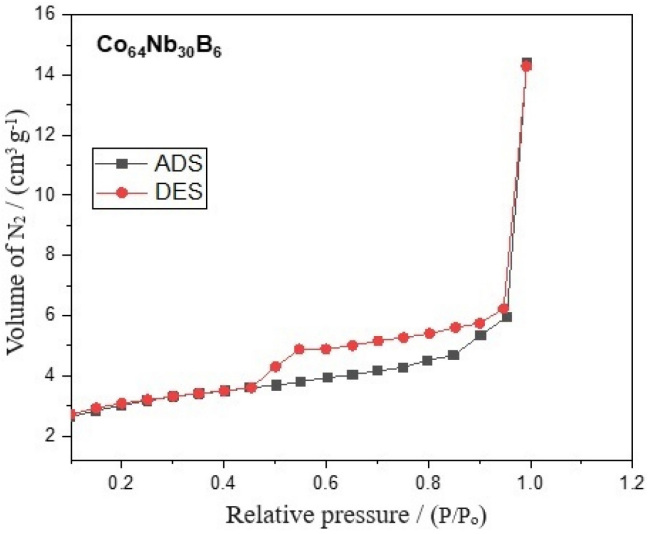

Figure 5. *Adsorption/desorption isotherms of N_2 for $Co_{64}Nb_{30}B_6$ alloy milled from 10 h*

classification.[49] A typical isotherm is observed for mesoporous solids and is characterized by a very pronounced hysteresis loop between the adsorption and desorption branches for the amorphous alloy $Co_{64}Nb_{30}B_6$. Furthermore, a very significant hysteresis can appear in the adsorption and desorption branches and does not return to the origin. Note that the isotherm of the amorphous alloy $Co_{64}Nb_{30}B_6$ has an inflection point in the hysteresis around P/P_o = 0.4-1, which is a typically excellent characteristic in the strong effect of mesoporosity and adsorption with desorption cycle in the range of P/P_o = 0.8-1, being related to a macropore phase.[50] A phase of mesopores with larger medium pores is observed in this same range of P/P_o = 0.8-1. The relative pressure (P/P_o) in the separated region in the adsorption and desorption curves was more significant than 0.8 in the $Co_{64}Nb_{30}B_6$ alloy, evidencing a larger pore diameter. The hysteresis was caused by the high capillary condensation that occurred in the mesopores. The hysteresis loop of type H3 is associated with non-rigid aggregates of plate-shaped particles originating slit pores.[51] These loops are attributed to materials that are often disordered where the distribution of pore size and shape is not well defined and also indicative of bottleneck constrictions.

CONCLUSIONS

Mechanical alloying has been used for 10 h for the amorphization of the powder of alloy $Co_{64}Nb_{30}B_6$. X-ray diffraction has shown that from 10 h of grinding, displayed in the 2θ range of 40-50° (2θ = 45°), presenting a typical diffuse halo and without any obvious diffraction peak corresponding to the crystalline phase, which implies a totally amorphous structure indicated within of the red circle, as shown in Figure 1. The micrographs obtained by SEM showed a snowflake agglomerate morphology within the size of approximately 50 μm milled for 10 h, respectively. However, the shape of the particles after 10 h of milling was snowflakes, and the EDS shows the distribution of chemical elements Co, Nb, and B in their most significant intensities. Through thermoanalytical analysis (TGA/DTA) of the $Co_{64}Nb_{30}B_6$ alloy, it was shown that at higher temperatures Co and Nb ions are oxidized by the environment and, therefore, the mass can be slightly increased to 14.9%, and a probable contribution of B in evolution stability thermal and magnetic in the amorphous phase. The amorphous alloy $Co_{64}Nb_{30}B_6$ exhibits good soft magnetic properties with one field coercivity for H_c = 28.68 kOe, remaining M_r = 0.00617 emu g^{-1} and present a low saturation magnetization

value of M_s = 0.2601 emu g^{-1} shows good soft magnetic properties, indicating a typical hysteresis loop for soft ferromagnetic materials. Finally, the N_2 adsorption-desorption isotherms of the $Co_{64}Nb_{30}B_6$ alloy present a type IV isotherm with a hysteresis loop profile characteristic of type H3 for mesoporous materials.

ACKNOWLEDGMENTS

The authors are thankful to the CAPES for their financial support and the Companhia Brasileira de Metalurgia e Mineração (CBMM).

REFERENCES

1. Faruq, M.; Villesuzanne, A.; Shao, G.; *J. Non-Cryst. Solids* **2018**, *487*, 72. [Crossref]
2. Dzhumazoda, A.; Panina, L. V.; Nematov, M. G.; Ukhasov, A. A.; Yudanov, N. A.; Morchenko, A. T.; Qin, F. X.; *J. Magn. Magn. Mater.* **2019**, *474*, 374. [Crossref]
3. Liu, X.; Bi, J.; Meng, Z.; Li, R.; Li, Y.; Zhang, T.; *Tribol. Int.* **2021**, *162*, 107142. [Crossref]
4. Permyakova, I.; Glezer, A.; *Metals* **2022**, *12*, 297. [Crossref]
5. Nowicki, M.; Gazda, P.; Szewczyk, R.; Marusenkov, A.; Nosenko, A.; Kyrylchuk, V.; *Acta Mater.* **2019**, *12*, 2110. [Crossref]
6. Kuś, A.; Pilarczyk, W.; Małachowska, A.; Ambroziak, A.; Gebara, P.; *Materials* **2021**, *14*, 7357. [Crossref]
7. Liu, C.; Li, Q.; Huo, J.; Yang, W.; Chang, L.; Chang, C.; Sun, Y.; *J. Magn. Magn. Mater.* **2018**, *446*, 162. [Crossref]
8. Corte-Leó, N. P.; Zhukova, V.; Ipatov, M.; Blanco, J. M.; Gonzalez, J.; Zhukov, A.; *Intermetallics* **2019**, *105*, 92. [Crossref]
9. Nykyruy, Y.; Mudry, S.; Shtablavyi, I.; Borisyuk, A.; Tsekhmister, Y.; Gnilitskyi, I.; *Mater. Chem. Phys.* **2022**, *287*, 126317. [Crossref]
10. Correa, M. A.; Ferreira, A.; Souza, A. L.; Dantas Neto, J. M.; Bohn, F.; Vaz, F.; Kurlyandskaya, G. V.; *Sensors* **2023**, *23*, 1420. [Crossref]
11. Eliaz, N.; *Materials* **2019**, *12*, 407. [Crossref]
12. Mahajan, A.; Sidhu, S. S.; *J. Mater. Res.* **2019**, *34*, 2837. [Crossref]
13. Nykyruy, Y.; Mudry, S.; Kulyk, Y.; Borisyuk, A.; *Appl. Nanosci.* **2023**, *13*, 5239. [Crossref]
14. Li, B. Y.; Li, A. C.; Zhao, S.; Meyers, M. A.; *Mater. Sci. Eng., R* **2022**, *149*, 100673. [Crossref]
15. Skulkina, N. A.; Ivanov, O. A.; Stepanova, E. A.; Blinova, O. V.; Kuznetsov, P. A.; Mazeeva, A. K.; *Phys. Met. Metallogr.* **2016**, *117*, 982. [Crossref]
16. Ghobrial, S.; Kirk, D. W.; Thorpe, S. J.; *J. Phys. Chem. Solids* **2018**, *502*, 1. [Crossref]
17. Nosenko, A. V.; Kyrylchuk, V. V.; Semen'ko, M. P.; Nowicki, M.; Marusenkov, A.; Mika, T. M.; Semyrg, M. O.; Zelinska, M. G.; Nosenko, V. K.; *Acta Mater.* **2020**, *515*, 167328. [Crossref]
18. Nematov, M. G.; Baraban, I.; Yudanov, N. A.; Rodionova, V.; Qin, F. X.; Peng, H. X.; Panina, L. V.; *J. Alloys Compd.* **2020**, *837*, 155584. [Crossref]
19. Li, K.; Wang, B.; Zhou, J.; Li, S. Y.; Huang, P. R.; *Colloids Surf., B* **2020**, *196*, 111251. [Crossref]
20. Zheng, Z. G.; Chen, Y. B.; Wei, J.; Wang, X.; Qiu, Z. G.; Zeng, D. C.; *J. Alloys Compd.* **2023**, *939*, 168621. [Crossref]
21. Shi, L.; Hu, X.; Li, Y.; Yuan, G.; Yao, K.; *Intermetallics* **2021**, *131*, 107116. [Crossref]
22. Popova, A. V.; Odintsov, V. I.; Kozlov, I. V.; Elmanov, G. N.; Kostitsyna, E. V.; Gorelikov, E. S.; Gudoshnikov, S. A.; *KnE Materials Science* **2018**, *4*, 323. [Crossref]
23. Nematov, M. G.; Baraban, I.; Yudanov, N. A.; Rodionova, V.; Qin, F. X.; Peng, H. X.; Panina, L. V.; *J. Alloys Compd.* **2020**, *837*, 155584. [Crossref]
24. Nykyruy, Y.; Mudry, S.; Kulyk, Y.; Prunitsa, V.; Borysiuk, A.; *J. Phys. Chem. Solids* **2023**, *24*, 106. [Crossref]
25. Yu, H.; Zhang, G.; Li, X.; Meng, L.; Dong, B.; Li, Z.; Zhou, S.; *J. Alloys Compd.* **2023**, *935*, 167895. [Crossref]
26. Gao, F.; Li, S.; Li, K.; *J. Alloys Compd.* **2020**, *826*, 154130. [Crossref]
27. Msetra, Z.; Khitouni, N.; Suñol, J. J.; Khitouni, M.; Chemingui, M.; *Mater. Lett.* **2021**, *292*, 129532. [Crossref]
28. Suryanarayana, C.; Al-Joubori, A. A.; Wang, Z.; *Met. Mater. Int.* **2022**, *28*, 41. [Crossref]
29. Srinivas, V.; Barua, P.; Murty, A. B.; *Mater. Sci. Eng., A* **2000**, *294*, 65. [Crossref]
30. Costa, F. A.; Silva, A. G. P.; Silva Júnior, J.; Gomes, U. U.; *Int. J. Refract. Hard Met.* **2018**, *26*, 499. [Crossref]
31. Lu, S.; Zhang, J.; Duan, H.; *Intermetallics* **2022**, *149*, 107674. [Crossref]
32. Li, J.; Zheng, J.; Wang, C.; He, A.; Dong, Y.; *J. Magn. Magn. Mater.* **2022**, *545*, 168771. [Crossref]
33. Binh, D. N.; Oanh, N. T. H.; Viet, N. H.; *Appl. Sci.* **2022**, *12*, 10561. [Crossref]
34. Wu, K. L.; Yu, R.; Li, X. Z.; Wei, X. W.; *Micro Nano Lett.* **2012**, *7*, 685. [Crossref]
35. Zhang, Y.; Czubayko, U.; Wanderka, N.; Zhu, F.; Wollenberger, H.; *J. Mater. Sci. Res.* **2000**, *15*, 1271. [Crossref]
36. Li, B. Y.; Li, A. C.; Zhao, S.; Meyers, M. A.; *Materials Science and Engineering: R: Reports* **2022**, *149*, 100673. [Crossref]
37. Feizabad, M. H. K.; Khayati, G. R.; Sharafi, S.; Ranjbar, M.; *J. Non-Cryst. Solids* **2018**, *493*, 11. [Crossref]
38. Guo, D.; Zhang, Y.; Geng, S.; Xu, H.; Ren, Z.; Wilde, G.; *J. Mater. Sci.* **2018**, *53*, 9816. [Crossref]
39. Louzguine-Luzgin, D. V.; Ivanov, Y. P.; Greer, A. L.; *J. Alloys Compd.* **2023**, *960*, 170618. [Crossref]
40. Li, X.; Wu, Y.; Yang, S.; Cha, X.; Shao, P.; Wang, L.; *J. Non-Cryst. Solids* **2019**, *503*, 284. [Crossref]
41. Masood, A.; Baghbaderani, H. A.; Ström, V.; Stamenov, P.; McCloskey, P.; Mathúna, C. O.; Kulkarni, S.; *J. Magn. Magn. Mater.* **2019**, *483*, 54. [Crossref]
42. Zhu, M.; Zhang, M.; Yao, L.; Nan, R.; Jian, Z.; Chang, F. E.; *Vaccum* **2019**, *163*, 368. [Crossref]
43. Gao, X.; Zhou, Y.; Cheng, Z.; Tan, Y.; Liu, S.; Shen, Z.; *Int. J. Hydrogen Energy* **2019**, *44*, 27421. [Crossref]
44. Machado, F. L. A.; Martins, C. S.; Rezende, S. M.; *Phys. Rev. B* **1995**, *51*, 3926. [Crossref]
45. Dong, X. Z.; Fernengel, W.; Kronmüller, H.; *Appl. Phys. A* **1982**, *28*, 103. [Crossref]
46. Zhang, Y.; Zhu, J.; Hao, Z.; Hao, W.; Mo, Z.; Li, L.; *Mater. Des.* **2023**, *229*, 111894. [Crossref]
47. Miao, B. W.; Luo, Q.; Chang, C. T.; Liu, T.; Zhang, Y.; Shen, *J. Magn. Magn. Mater.* **2019**, *477*, 156. [Crossref]
48. Wang, F.; Inoue, A.; Han, Y.; Kong, F. L.; Zhu, S. L.; Shalaan, E.; Al-Marzouki, F.; Obaid, A.; *J. Alloys Compd.* **2017**, *711*, 132. [Crossref]
49. Thommes, M.; Kaneko, K.; Neimark, A. V.; Olivier, J. P.; Rodriguez-Reinoso, F.; Rouquerol, J.; Sing, K. S. P.; *Pure Appl. Chem.* **2015**, *87*, 1051. [Crossref]
50. Toncón-Leal, C. F.; Villarroel-Rocha, J.; Silva, M. T. P. D.; Braga, T. P.; Sapag, K.; *Adsorption* **2021**, *27*, 1109. [Crossref]
51. Okonye, L. U.; Yao, Y.; Hildebrandt, D.; Meijboom, R.; *Sustainable Energy Fuels* **2021**, *5*, 79. [Crossref]